Mathematical Modeling and Validation of Saturating and Clampable Cascaded Magnetics for Magnetic Energy Harvesting

Min Gao, *Student Member, IEEE*, Lifang Yi, *Student Member, IEEE*, and Jinyeong Moon, *Senior Member, IEEE*

***Abstract*—Electromagnetic energy harvesting extracts energy from magnetic fields and can provide power to sensors, monitoring nodes, cyber-physical systems and control elements without additional battery and external power source and wiring. This article presents a novel ac-driven electromagnetic energy harvester based on periodically saturating, cascaded magnetics, consisting of a clampable magnetic core and an ungapped high permeability core. The high permeability core guarantees the maximum energy extraction, whereas the clampable core enables the nonintrusive installation of the energy harvester for more pervasive applications. This article first builds a comprehensive mathematical model based on this saturating cascaded magnetic structure, considering the reachability of an individual saturation flux density of the two magnetic cores. This model resolves the new challenges introduced by the cascaded magnetics with respect to a traditional single-core case, providing the accurate calculation of the lengths of the relevant time windows for harvesting and the amount of the harvested power. Our mathematical model is verified against simulation and experiment, showing excellent agreement among them with the maximum discrepancy of less than 6%. This article also reveals that the maximum power extraction occurs when the ungapped core operates in its slightly saturated state and that the harvested power increases with a higher primary current as well as a higher line frequency.**

***Index Terms*—AC-driven, cascaded, magnetic core, electromagnetic, energy, harvesting, magnetics, saturation.**

I. Introduction

ENERGY harvesting (EH) is a process of converting ambient energy into usable electrical energy. The applications of EH strongly depend on the scale of the harvestable energy. Large-scale sources, such as solar, wind, and biomass energy, can reach power levels up to MW, and serve as active, renewable energy sources for power grid [1]. Small-scale energy sources, such as piezoelectric [2], [3], radio frequency (RF) [4], [5], thermal gradients [6], [7], vibration [8], [9], [10], [11], and human motions [12], can be utilized to supply power to environmental sensors [13], healthcare monitoring nodes [14], Internet-of-Things (IoT) or cyber-physical systems (CPS) [15], and data networking devices [16] without customized wiring, batteries, and additional line-interfacing power electronics. If complemented by an energy storage system (ESS) (e.g., battery, capacitors) at the expense of increased cost, complexity, and size, energy harvesters can greatly improve the reliability of the end application.

However, energy sources often lead to a design complication and present a risk in the feasibility of an EH node. For example, the energy output of photovoltaic (PV) energy harvesters is dependent on solar irradiance, which is negligible at night and fractionally low during cloudy or rainy days. Thermoelectric and RF energy harvesters require a large area or space, resulting in relatively low power densities. Piezoelectric energy harvesters are usually suitable for a low output current application and generally rely on unpredictable mechanical pressure. For traditional vibration-based energy harvesters, costly and brittle permanent magnets are necessary and they are also subject to the unpredictable nature of vibration or kinetic motion of magnets [10], [11]. In addition, its output voltage is low (i.e., several hundreds of mV) unless coils with a very large number ($>$2000) of turns are used [17], necessitating a step-up conversion to achieve usable voltages for microcontrollers, wireless transmitter, etc. In [18], an inductor-less converter is utilized to boost the low ac voltage generated by a vibration-based energy harvester to a nominal dc voltage. The conventional boost and buck–boost topologies are integrated in [19] and [20] for low-voltage EH applications. Additional step-up conversions complicate vibration-based energy harvesters, putting them at cost and power density disadvantages.

Compared to vibration-based electromagnetic energy harvesters, ac-driven electromagnetic energy harvesters can generate relatively high output voltage and power [21], which have better controllability and predictability in energy extraction and do not require permanent magnets [21], [22], [23]. A single toroidal magnetic core with a high permeability is utilized in [21], extracting energy from an ac current-induced magnetic field to power the sensor system without a boost converter. Detailed mathematical models are developed to predict and optimize the harvested power. The relationship between the primary current and output voltage of this type of EH is further discussed in [24]. A new method is proposed in [25] to boost the

Manuscript received 15 July 2022; revised 22 September 2022; accepted 29 October 2022. Date of publication 1 November 2022; date of current version 26 December 2022. Recommended for publication by Associate Editor K.-H. Chen. *(Corresponding author: Min Gao.)*

The authors are with the Department of Electrical and Computer Engineering, Florida State University, Tallahassee, FL 32310 USA (e-mail: mgao@fsu.edu; lyi@fsu.edu; j.moon@fsu.edu).

Color versions of one or more figures in this article are available at https://doi.org/10.1109/TPEL.2022.3218725.

Digital Object Identifier 10.1109/TPEL.2022.3218725

harvestable power for a resistively loaded, saturated single-core case by adding an additional coil and manipulating the magnetic field generated by the primary. In [26], a capacitor and two switches are used to boost the harvested power and store energy at the same time, showing good results at low primary currents. However, the single toroidal core makes it challenging to retrofit into an existing system without breaking the current-carrying wire of the primary system unless the core is integrated into the system at the initial design stage [27].

Otherwise, a magnetic core consisting of two halves is required to clamp on the current-carrying wire for installation. A dual wire current transformer based on a gapped core [28] is used to achieve EH and power a sensor monitoring system. In [29], energy harvesters based on two gapped cores are installed on transmission lines and the performance of three different air gaps is discussed. Though the gapped cores in these works enhance the nonintrusiveness of the installation, high permeability, magnetic saturation, and their beneficial roles in the harvested power are not explored nor exploited for improved performance.

In this article, a two-stage cascaded magnetic structure, consisting of a clampable core in tandem with an ungapped core, is proposed. A clampable core is used in the first stage to facilitate a nonintrusive mounting of the energy harvester onto the current-carrying wire. An ungapped toroidal core with a high permeability is then cascaded as the second magnetic stage to maximize the harvested power. The primary advantage of this two-stage cascaded structure is to open a door for electromagnetic EH to be employed in a wide range of applications with the aid of a clampable core avoiding the downtime of the mother system. The second advantage of the two-core structure is that the power extraction can be still drastically enhanced via utilizing a high permeability core, subject to the structural (two-core) constraint. To predict the harvested power accurately based on the two-core structure connected to a practical constant voltage load (e.g., battery, supercapacitor, or input stage of a subsequent power conversion), a new mathematical model for multiple cores, potential magnetic saturation, and existence of air gaps is required beyond the single toroidal core case.

The rest of this article is organized as follows. The fundamentals of electromagnetic EH are introduced in Section II. The detailed mathematical modeling and operational principles of our approach with nonlinear considerations for the cascaded cores are presented in Section III, followed by simulation and experiment verification in Section IV.

II. Background and Existing Work

A. Electromagnetic EH Basics: Single-Core

The electromagnetic EH is based on magnetic fields induced by an ac current, as shown in Fig. 1. An ac current in the primary wire generates time-varying magnetic fields in the magnetic core, inducing voltage across the secondary winding terminals. Unlike a current transformer, conventionally used for current measurement based on a nonsaturating magnetic core with good linearity, the magnetic core used in this case is intentionally saturated every ac cycle at an opportune time for maximum energy extraction [21], [22].

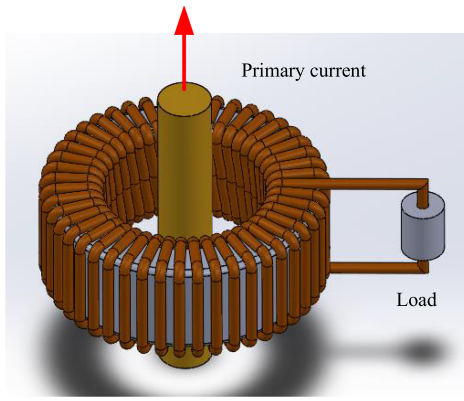

Fig. 1. Single-core case.

B. Maximum Output Power Derivation

Under the constant voltage load condition in which a rectifier is inserted between the secondary winding and load shown in Fig. 1, the unsaturated time duration (i.e., $0 < t < t_{\text{SAT}}$) is determined by the core characteristics, such as the maximum magnetic flux density (B_{SAT}), core cross-sectional area (A_{CORE}), number of turns on the secondary winding (N), and load voltage (V_{LOAD}), as expressed as follows.

$$2B_{\text{SAT}}A_{\text{CORE}}N = \int_0^{t_{\text{SAT}}} V_{\text{LOAD}}\,\mathrm{d}t. \tag{1}$$

When solved, (1) becomes

$$t_{\text{SAT}} = \min\left[\frac{2B_{\text{SAT}}A_{\text{CORE}}N}{V_{\text{LOAD}}}, \frac{T}{2}\right]. \tag{2}$$

Here, T is the period of the primary current. If t_{SAT} is larger than the half of the period, the core entirely operates in the unsaturated state and t_{SAT} will be capped at $T/2$.

The average harvested power then can be expressed as

$$\begin{aligned} P_{\text{LOAD}} &= \frac{2}{T}\int_0^{t_{\text{SAT}}} \left[\frac{I_P}{N}\sin(\omega t)\right] V_{\text{LOAD}}\,\mathrm{d}t \\ &= \frac{I_P V_{\text{LOAD}}}{\pi N}\left[1-\cos(\omega t_{\text{SAT}})\right]. \end{aligned} \tag{3}$$

Here, I_P is the peak amplitude of the ac current on the primary side that generates magnetic fields. If the core is never saturated (i.e., $t_{\text{SAT}} = T/2$), the load power simplifies to

$$P_{\text{LOAD,unsat}} = \frac{2I_P V_{\text{LOAD}}}{\pi N}. \tag{4}$$

In this case, the average load power is a monotonically increasing function of the load voltage. This is an intuitive behavior as the configuration is essentially a perfect current transformer that outputs the same current regardless of the load voltage. On the other hand, if the magnetic core enters saturation mid-cycle, the average harvested power becomes

$$P_{\text{LOAD,sat}} = \frac{2\omega B_{\text{SAT}}A_{\text{CORE}}I_P}{\pi}\cdot\frac{(1-\cos(\omega t_{\text{SAT}}))}{\omega t_{\text{SAT}}}. \tag{5}$$

The first part in (5) is a constant. The second part, which can be seen as $\frac{1-\cos(x)}{x}$, is a function with a maxima, as shown in

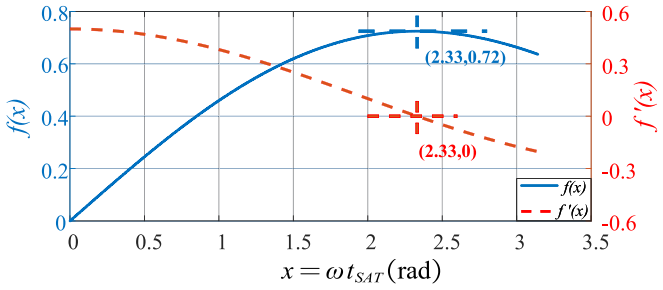

Fig. 2. Response of $f(x) = \frac{1-\cos(x)}{x}$ and $f'(x)$.

solid blue in Fig. 2. The maximally harvestable power therefore occurs at the peak of $f(x)$ (i.e., $\omega t_{\text{SAT}} = 2.33$ or equivalently $t_{\text{SAT}} = 0.371\,T$). Because this t_{SAT} value is less than $T/2$, this maximum power point implies a mid-cycle magnetic saturation, with the harvested power level exceeding the unsaturated case, $P_{\text{LOAD,unsat}}$. This is the counter-intuitive, but beneficial effect of involving a saturating magnetic core in an EH application [21] with the maximum harvested power being approximately

$$P_{\text{LOAD,max}} = \frac{8\left(2+\sqrt{2}\right)}{6\pi^2}\omega I_P B_{\text{SAT}} A_{\text{CORE}}. \tag{6}$$

The most important requirement for a magnetic core to avail this approach is an extremely high magnetic permeability (e.g., $\mu_r = 262,488$ in [21]). This is to guarantee a development of a usable voltage (i.e., more than a few volts) on the secondary winding at the line frequency (i.e., 50 Hz or 60 Hz) without additional power electronics. In addition, a high permeability core can also help deliver higher power to the load side as the core with a higher permeability will exhibit larger magnetizing inductance and shunt impedance. As the core becomes more ideal, the coupled current will naturally favor the load, compared to the shunt impedance, to flow, increasing the harvested power in the load. With a magnetic permeability reaching hundreds of thousands like [21] and in this article, the core will be a near-ideal current transformer during the transfer window. This exact reason actually eliminates the necessity of impedance matching between the core and the load in our design—the core's shunt impedance is orders of magnitude larger than the load when the magnetic core is not saturated. Hence, most of the "harvested current" will flow through the load. The drawback of requiring an extremely high magnetic permeability is that a pristine ungapped magnetic core must be used, as a clampable core cannot provide such a high level of permeability. Therefore, the installation of a single-core harvester must consider the intrusiveness of the installation at the design phase as the harvester cannot be integrated into an existing system without breaking the wire connection of the primary system, forcing a downtime of the primary.

One potential solution to these single core issues—intrusiveness of a high permeability core and low permeability in a clampable core—is a two-core structure, a combination of a clampable core and an ungapped core. The first magnetic stage will be a clampable core to ease the intrusiveness in

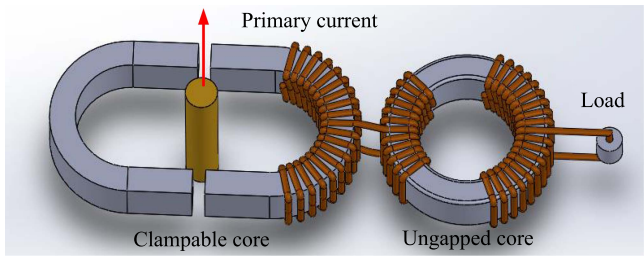

Fig. 3. Structure for two-core cascade magnetic harvesting.

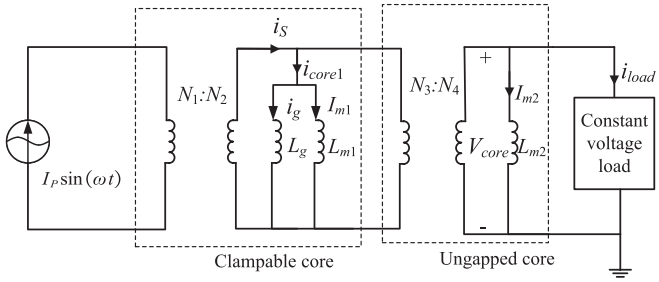

Fig. 4. Equivalent circuit model of cascaded magnetic cores.

installation. The second stage will be an ungapped core with an extremely high magnetic permeability for high shunt impedance and easily controllable magnetic saturation for maximum energy extraction. However, it is still expected in a two-core approach that the air gap in the first stage will nonetheless reduce the "overall" permeability of the entire magnetics and affect the energy extraction. This is the price of easier installation.

III. Two-Core Cascade Magnetics

A. Definitions for the Proposed Mathematical Modeling

The two-core structure is depicted in Fig. 3. The current-carrying wire of the primary side is presented as the single thick winding on the left. A clampable core with gaps, consisting of two halves, wraps around the primary winding, creating a magnetic coupling, and transferring flux to the second core on the right side. The second core is ungapped with an extremely high magnetic permeability and connected to the subsequent power electronic circuits (e.g., a rectifier) and loads. This structure will enable a nonintrusive system integration and utilize the characteristics of a high permeability core for maximum energy extraction.

In Fig. 4, an ungapped high permeability core is modeled as an ideal transformer in parallel with a magnetizing inductance, L_{m2}. This L_{m2} is highly nonlinear because of the variable permeability changing from an extremely large value when unsaturated to a negligible value when saturated. The model of a clampable core, also shown in Fig. 4, is an ideal transformer in parallel with a linear inductor, L_g, that represents an air gap inductance and a nonlinear magnetizing inductance, L_{m1}.

In this analysis, the magnetic path lengths, permeabilities, maximum magnetic flux densities, and cross-sectional areas of the clampable and ungapped cores are denoted as l_{m1}, l_{m2},

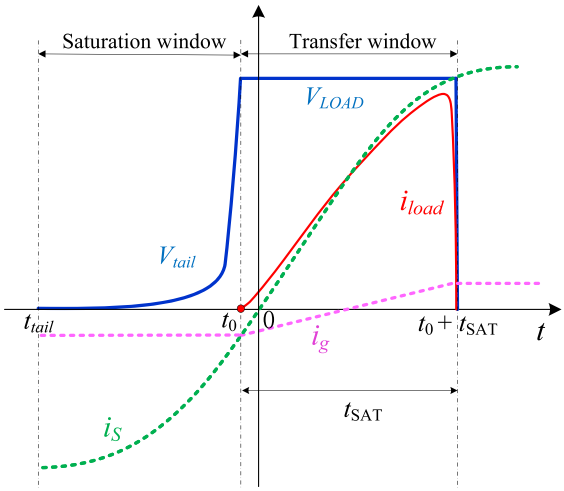

Fig. 5. Waveforms of the core voltage, source current (reflected to the secondary side of the gapped core), gapped core current, and load current.

μ_{r1}, μ_{r2}, B_{SAT1}, B_{SAT2}, A_{CORE1}, and A_{CORE2}, respectively. The numbers of turns in windings on the clampable and ungapped cores are N_1, N_2, N_3, and N_4, respectively, and denoted on the ideal transformers in Fig. 4. If neither of the cores is saturated, the magnetizing inductances of the two cores, L_{m1} and L_{m2}, can be considered nearly constant. The existence of L_g implies an existence of flux leakage from the air gap. The ungapped core, however, has an extremely high magnetic permeability with negligible flux leakage. Therefore, the leakage current for the ungapped core is neglected.

Fig. 5 shows the waveforms of the load current, i_{load}, air gap inductance current, i_g, secondary transformer current of the clampable core, i_S, and voltage across the ungapped magnetic core seen from the load side (i.e., V_{tail} in the "Saturation window" and V_{LOAD} in the "Transfer window," as defined in Fig. 5—they will be collectively referred to as V_{core}). The detailed steps to get the expressions of V_{tail} and i_g, which depend on the core parameters (i.e., permeability, maximum magnetic field density, magnetic path length, and cross-sectional area), air gap inductance, winding turns, load voltage, and primary current magnitude and frequency, will be presented in the next part. At the beginning of each cycle, the core starts from its unsaturated state, exhibiting high permeability and high shunt impedance. The core during this time behaves as a near-ideal current source as most of the transformer current will avoid the high shunt impedance and flow into the load. This is when the power is extracted and transferred to the load. Eventually, the accumulated magnetic flux reaches the critical level, and the core enters magnetic saturation. Once the core is saturated, power extraction and transfer essentially stop as the voltage across the core cannot be developed. Because of the polarity reversal of the current source, the core comes out of the saturation and generates an inverse tail voltage. Hence, each half cycle is divided into two windows. One is the power transfer window when the core is not saturated and current can be delivered to the load side. The other is the saturation window when the core is saturated and no power is delivered. The transfer window begins when the load current increases from zero and ends when the load current decreases to zero. During the transfer window, the core voltage is equal to the load voltage. On the other hand, during the saturation window, the core voltage has a tail caused by a polarity reversal of the current source and the core coming out of the saturation correspondingly. Although the tail voltage is critical in the calculation of the saturation window, such consideration has never been done analytically due to the calculation complexity. This article will be the first work to derive the analytical result.

The lengths of the transfer windows of the clampable and ungapped cores are independently denoted as t_{SAT1} and t_{SAT2}, respectively. An individual transfer window is still capped at $T/2$. The length of the overall transfer window, t_{SAT}, of the entire magnetic structure will be the minimum value of t_{SAT1}, t_{SAT2}, and $T/2$. Our paper's new contribution to the field will be the prediction of energy extraction with respect to the dynamic situations of individual saturation levels.

B. Ideal Mathematical Modeling of the Cascade Magnetics

The objective of this section is to calculate the three important timing parameters that describe the magnetic saturation and determine the level of harvested power. The first parameter, t_0, designates the starting point of the transfer window, which begins when the load current increases from zero. The second parameter, t_{SAT}, is the length of the transfer window. The third parameter, t_{tail}, is defined as the time point at which the voltage across the magnetic core changes its direction and rises from zero during magnetic saturation.

The internal current of the clampable core, $i_{\text{core1}}(t)$, can be approximated to its air gap current, $i_g(t)$, if the core operates far away from saturation. This is because in such a situation, the magnetizing inductance is far larger than the air gap inductance (i.e., $L_g \ll L_{m1}$). Almost all current flows through the air gap inductance. In such a case

$$i_{\text{core1}}(t) \approx\ i_g(t) = \int \frac{N_3}{N_4}\frac{V_{\text{core}}(t)}{L_g}\mathrm{d}t. \tag{7}$$

Then, $i_g(t)$ for $t \in [t_{\text{tail}}, t_0]$ can be written as

$$i_g(t) = i_g\left(t_{\text{tail}}\right) + \int_{t_{\text{tail}}}^{t} \frac{N_3 V_{\text{tail}}(t)}{N_4 L_g}\mathrm{d}t \tag{8}$$

and $i_g(t)$ for $t \in [t_0, t_0 + t_{\text{SAT}}]$ can be written as

$$i_g(t) = i_g\left(t_{\text{tail}}\right) + \int_{t_{\text{tail}}}^{t_0} \frac{N_3 V_{\text{tail}}(t)}{N_4 L_g}\mathrm{d}t + \int_{t_0}^{t} \frac{N_3 V_{\text{LOAD}}}{N_4 L_g}\mathrm{d}t. \tag{9}$$

Here, t_{tail} is the time point, where the voltage across the ungapped core increases from zero while the magnetic field in the ungapped core changes its direction. Denoted as t_0 is the endpoint of the saturation window and start-point of the transfer window, where the load current begins to increase from zero and $V_{\text{core}}(t)$ reaches the load voltage, V_{LOAD}.

Since $i_g(t)$ must be half-wave symmetric in ac steady state

$$i_g\left(t_{\text{tail}}\right) = -i_g\left(t_{\text{tail}} + \frac{T}{2}\right). \tag{10}$$

Here, the left-hand side of (10) will be computed with (8) and the right-hand side will be computed with (9). When it is solved, the swing amplitude of the air gap current, $i_g(t_{\text{tail}})$, is obtained

$$i_g\left(t_{\text{tail}}\right) = -\frac{N_3}{2N_4L_g}\left(V_{\text{LOAD}}t_{\text{SAT}} + \int_{t_{\text{tail}}}^{t_0} V_{\text{tail}}(t)\mathrm{d}t\right). \quad (11)$$

Now, there can be two cases for t_{SAT}. The first case is when the magnetic flux density (B-field) inside the ungapped core reaches the saturation level (i.e., B_{SAT2}) before the B-field in the clampable core does, making $t_{\text{SAT}} = t_{\text{SAT2}}$. The second case is when the opposite happens, making $t_{\text{SAT}} = t_{\text{SAT1}}$.

1) Case 1: B_{SAT2} Occurs First ($t_{\text{SAT}} = t_{\text{SAT2}}$): If the ungapped core is saturated first, t_{SAT2} is determined according to Faraday's Law

$$2B_{\text{SAT2}}A_{\text{CORE2}}N_4 = \int_{t_{\text{tail}}}^{t_0} V_{\text{tail}}(t)\mathrm{d}t + V_{\text{LOAD}}t_{\text{SAT2}}. \quad (12)$$

Combining (12), (11), and (8), the updated expression for $i_g(t)$ during the saturation window (i.e., $t \in [t_{\text{tail}}, t_0]$) is obtained in terms of provided parameters

$$i_g(t) = -\frac{B_{\text{SAT2}}A_{\text{CORE2}}N_3}{L_g} + \int_{t_{\text{tail}}}^{t} \frac{N_3V_{\text{tail}}(t)}{N_4L_g}\,\mathrm{d}t. \quad (13)$$

The KCL at the top node of the middle circuit in Fig. 4 can be expressed as follows:

$$\begin{aligned}\frac{N_1}{N_2}I_P\sin(\omega t) &= i_{\text{core1}}(t) + \frac{N_4}{N_3}i_{\text{load}}(t) + \frac{N_4}{N_3}I_{m2}(t)\\ &\approx i_g(t) + \frac{N_4}{N_3}i_{\text{load}}(t) + \frac{N_4}{N_3}I_{m2}(t). \quad (14)\end{aligned}$$

During the saturation window, $i_{\text{load}}(t)$ is negligibly small. Then, by combining (14) and (13), the current through L_{m2} (i.e., $I_{m2}(t)$) during the saturation window (i.e., $t \in [t_{\text{tail}}, t_0]$) is obtained

$$\begin{aligned}I_{m2}(t) = &\frac{N_1N_3}{N_2N_4}I_P\sin(\omega t) + \frac{B_{\text{SAT2}}A_{\text{CORE2}}N_3^2}{L_gN_4}\\ &- \int_{t_{\text{tail}}}^{t} \frac{N_3^2V_{\text{tail}}(t)}{N_4^2L_g}\,\mathrm{d}t. \quad (15)\end{aligned}$$

By applying Ampere's law to (15) at the radius for l_{m2} (i.e., near the center), the H-field in the ungapped core during the saturation window (i.e., $(t \in [t_{\text{tail}}, t_0])$) can be expressed as

$$H_2(t) = \frac{N_4}{l_{m2}}I_{m2}(t). \quad (16)$$

To convert this H-field into the B-field, the mathematical function for the B–H curve must be chosen [30], [31], [32]. In this article, the "arctan" function that performed well in [21] is chosen

$$B_2(t) = B_{\text{SAT2}} \cdot \frac{2}{\pi}\arctan\left(\frac{H_2(t)}{\delta}\right). \quad (17)$$

Here, δ is a scaled reciprocal of the initial permeability as calculated below. Differentiating both sides of (17) with respect to H_2 yields the expression for the time-varying magnetic permeability during the saturation window

$$\mu_2(t) = \frac{\partial B_2(t)}{\partial H_2(t)} = \frac{2B_{\text{SAT2}}}{\pi\delta} \cdot \cos^2\left(\frac{\pi}{2} \cdot \frac{B_2}{B_{\text{SAT2}}}\right). \quad (18)$$

When evaluated at $B_2 = 0$, this expression provides the initial magnetic permeability, $\mu_{r2}\mu_0$, where μ_0 is the permeability of free space ($\mu_0 = 4\pi \times 10^{-7}$ Hm^{-1})

$$\mu_{r2}\mu_0 = \frac{2B_{\text{SAT2}}}{\pi\delta} \cdot \cos^2(0) = \frac{2B_{\text{SAT2}}}{\pi\delta}. \quad (19)$$

Therefore, δ is a scaled reciprocal of the permeability

$$\delta = \frac{B_{\text{SAT2}}}{\mu_{r2}\mu_0} \cdot \frac{2}{\pi}. \quad (20)$$

Then, combining (20), (17), and (16) yields the time-varying B-field inside the ungapped core with mid-cycle saturation

$$B_2(t) = \frac{2B_{\text{SAT2}}}{\pi} \cdot \arctan\left(\frac{\pi\mu_{r2}\mu_0}{2B_{\text{SAT2}}} \cdot \frac{N_4}{l_{m2}}I_{m2}(t)\right). \quad (21)$$

Meanwhile, during the saturation window (i.e., $t \in [t_{\text{tail}}, t_0]$), the ungapped core is in saturation with the B-field level close to B_{SAT2} and slowly coming out of saturation toward t_0. The tail voltage will work against this existing B-field as the polarity of the tail voltage is opposite to that of the voltage that drove the core into saturation in the previous half cycle. During this time, the internal B-field of the ungapped core can also be written as

$$B_2(t) = B_{\text{SAT2}} - \int_{t_{\text{tail}}}^{t} \frac{V_{\text{tail}}(t)}{A_{\text{CORE2}}N_4}\mathrm{d}t. \quad (22)$$

By taking the time derivative of (22), Faraday's law of induction during the saturation window can be confirmed

$$V_{\text{tail}}(t) = A_{\text{CORE2}}N_4\frac{dB_2(t)}{\mathrm{d}t}. \quad (23)$$

Merging this circuit constraint, (23), with the core material's property, (21), and the definition of $I_{m2}(t)$, (15), a single-variable equation about $V_{\text{tail}}(t)$ is obtained

$$\begin{aligned}&V_{\text{tail}}(t)\\ &= \frac{\mu_{r2}\mu_0A_{\text{CORE2}}N_4 \cdot \left(\frac{N_1N_3I_P\omega}{N_2l_{m2}}\cos(\omega t) - \frac{N_3^2V_{\text{tail}}(t)}{L_gl_{m2}N_4}\right)}{\left(\frac{\mu_{r2}\mu_0\pi}{2B_{\text{SAT2}}} \cdot \left(\frac{N_1N_3}{N_2l_{m2}}I_P\sin(\omega t) + \frac{B_{\text{SAT2}}A_{\text{CORE2}}N_3^2}{L_gl_{m2}}\right)\right)^2 + 1}. \quad (24)\end{aligned}$$

While obtaining (24), an ideal assumption is made that the change in the air gap current (i.e., Δi_g) is negligibly small during the saturation window, which might occur because of a likely combination of large L_g, large N_4, or small N_3. This is also to get a simpler response first without a transcendental differential equation. This assumption leads (24) to an explicit linear equation of $V_{\text{tail}}(t)$. The assumption will be subsequently removed to explore the general response.

When (24) is solved, the expression of $V_{\text{tail}}(t)$ is

$$V_{\text{tail}}(t) = \frac{A_2\cos(\omega t)}{\left(C_2\sin(\omega t) + D_2\right)^2 + 1 + E_2} \quad (25)$$

where

$$A_2 = \frac{\mu_{r2}\mu_0 A_{\text{CORE2}} N_4 N_1 N_3 I_P \omega}{l_{m2} N_2}$$

$$C_2 = \frac{\mu_{r2}\mu_0 \pi N_1 N_3 I_P}{2B_{\text{SAT2}} l_{m2} N_2}$$

$$D_2 = \frac{\mu_{r2}\mu_0 \pi A_{\text{CORE2}} N_3^2}{2L_g l_{m2}}$$

$$E_2 = \frac{\mu_{r2}\mu_0 A_{\text{CORE2}} N_3^2}{L_g l_{m2}}. \tag{26}$$

The first important timing parameter, t_0, can be calculated by considering the voltage condition at the end-point of the saturation window since the voltage across the ungapped core at $t = t_0$ must reach V_{LOAD}. Therefore, t_0 can be obtained by solving this condition

$$V_{\text{tail}}(t_0) = V_{\text{LOAD}}. \tag{27}$$

To calculate the second important timing parameter, t_{SAT2}, the equations (25) and (12) can be combined to yield

$$t_{\text{SAT2}} = \frac{2B_{\text{SAT2}} A_{\text{CORE2}} N_4 - \int_{t_{\text{tail}}}^{t_0} V_{\text{tail}}(\tau)\,\mathrm{d}\tau}{V_{\text{LOAD}}}. \tag{28}$$

The integration in (28) needs to be evaluated. It can be done by substituting (21) and (15) into (22) and testing at $t = t_0$. The result is

$$\int_{t_{\text{tail}}}^{t_0} V_{\text{tail}}(\tau)\,\mathrm{d}\tau = B_{\text{SAT2}} A_{\text{CORE2}} N_4 \left(1 - \frac{2}{\pi}\arctan\left(C_2 \sin(\omega t_0) + D_2\right)\right). \tag{29}$$

Plugging (29) back into (28), t_{SAT2} is obtained

$$t_{\text{SAT2}} = \frac{B_{\text{SAT2}} A_{\text{CORE2}} N_4}{V_{\text{LOAD}}} \left(1 + \frac{2}{\pi}\arctan\left(C_2 \sin(\omega t_0) + D_2\right)\right). \tag{30}$$

Finally, the last parameter, t_{tail}, can be similarly obtained with a voltage condition at $t = t_{\text{tail}}$. Based on the level of magnetic saturation, a suitable voltage level must be equated. For example, in a relatively heavy saturation case, where t_{tail} is the first time point that the voltage across the ungapped core is rising from zero, the condition will be $V_{\text{tail}}(t_{\text{tail}}) = 0$, resulting in $t_{\text{tail}} = -T/4$.

On the other hand, in a relatively soft saturation case, where the transfer window of the previous half cycle protrudes past $t = -T/4$, the value of t_{tail} will be set to the actual end-point of the previous transfer window, $t_{\text{tail}} = t_{\text{SAT2}} + t_0 - T/2$. Therefore

$$t_{\text{tail}} = \max\left[t_{\text{SAT2}} + t_0 - \frac{T}{2}, -\frac{T}{4}\right]. \tag{31}$$

The calculated t_0, t_{SAT2}, and t_{tail} will predict when and how the ungapped core recovers from saturation and when it goes into saturation again in this half cycle.

2) Case 2: B_{SAT1} Occurs First ($t_{\text{SAT}} = t_{\text{SAT1}}$): For the case where the B-field inside the clampable core reaches the saturation level, B_{SAT1}, before the B-field inside the ungapped core reaches B_{SAT2}, the expression of $V_{\text{tail}}(t)$ can be similarly derived as the previous case

$$V_{\text{tail}}(t) = \frac{A_1 \cos(\omega t)}{\left(C_1 \sin(\omega t) + D_1\right)^2 + 1 + E_1} \tag{32}$$

where

$$A_1 = \frac{\mu_{r1}\mu_0 A_{\text{CORE1}} N_4 N_1 N_2 I_P \omega}{l_{m1} N_3}$$

$$C_1 = \frac{\mu_{r1}\mu_0 \pi N_1 I_P}{2B_{\text{SAT1}} l_{m1}}$$

$$D_1 = \frac{\mu_{r1}\mu_0 \pi A_{\text{CORE1}} N_2^2}{2L_g l_{m1}}$$

$$E_1 = \frac{\mu_{r1}\mu_0 A_{\text{CORE1}} N_2^2}{L_g l_{m1}}. \tag{33}$$

Again, t_0 is identically obtained using (27). A similar flux balance equation to (28) yields t_{SAT1} as follows:

$$t_{\text{SAT1}} = \frac{B_{\text{SAT1}} A_{\text{CORE1}} N_4 N_2}{V_{\text{LOAD}} N_3} \left(1 + \frac{2}{\pi}\arctan\left(C_1 \sin(\omega t_0) + D_1\right)\right). \tag{34}$$

Once t_{SAT1} and t_{SAT2} are individually calculated using the results in these two cases, the transfer window for the two-core case can be finally computed with the "min" function

$$t_{\text{SAT}} = \min\left[t_{\text{SAT1}},\ t_{\text{SAT2}},\ \frac{T}{2}\right]. \tag{35}$$

t_0 and t_{tail} will be accordingly selected based on the case.

C. Nonlinearity Consideration: Δi_g During Saturation

Unlike the previous assumption made for (24), if the change in the air gap current, Δi_g, can not be ignored during the saturation window, it can be shown that (25) becomes a transcendental differential equation as below, instead of being an explicit solution for $V_{\text{tail}}(t)$

$$V_{\text{tail}}(t) = \frac{A_i \cos(\omega t)}{\left(C_i \sin(\omega t) + D_i - F_i \int_{t_{\text{tail}}}^{t} V_{\text{tail}}(\tau)\,\mathrm{d}\tau\right)^2 + 1 + E_i} \tag{36}$$

where A_i, C_i, D_i, and E_i remain the same and

$$F_1 = \frac{\mu_{r2}\mu_0 \pi N_3^2}{2B_{\text{SAT2}} L_g l_{m2} N_4} \quad (\text{if } t_{\text{SAT}} = t_{\text{SAT2}}) \tag{37}$$

or

$$F_2 = \frac{\mu_{r1}\mu_0 \pi N_3 N_2}{2B_{\text{SAT1}} L_g l_{m1} N_4} \quad (\text{if } t_{\text{SAT}} = t_{\text{SAT1}}). \tag{38}$$

This modified equation will compute an accurate set of new t_0, t_{tail}, and t_{SAT} without an assumption on Δi_g. The main challenge

is to calculate the value of the integral at $t = t_0$ and solve t_0 according to (27).

To calculate t_0 in this new setting, (22) is rearranged and evaluated at $t = t_0$ first

$$\int_{t_{\text{tail}}}^{t_0} V_{\text{tail}}(\tau)\,\mathrm{d}\tau = A_{\text{CORE2}} N_4 \left(B_{\text{SAT2}} - B_2(t_0)\right). \tag{39}$$

Here, $B_2(t_0)$ can be eliminated by substituting (21) and (15) into (39). Then, using the definitions of the various coefficients provided in (26), it can be readily shown that

$$\int_{t_{\text{tail}}}^{t_0} V_{\text{tail}}(\tau)\,\mathrm{d}\tau = B_{\text{SAT2}} A_{\text{CORE2}} N_4 \times \left(1 - \frac{2}{\pi}\arctan\sqrt{\frac{A_2\cos(\omega t_0)}{V_{\text{LOAD}}} - 1 - E_2}\right). \tag{40}$$

Now that the integral is expressed in terms of the coefficients and t_0, (36) can now be evaluated at $t = t_0$. Then, the voltage condition at t_0 (i.e., $V_{\text{tail}}(t_0) = V_{\text{LOAD}}$) can be written as

$$V_{\text{LOAD}} = \frac{A_2\cos(\omega t_0)}{\left(C_2\sin(\omega t_0) + E_2\arctan\sqrt{\dfrac{A_2\cos(\omega t_0)}{V_{LOAD}} - 1 - E_2}\right)^2 + 1 + E_2}. \tag{41}$$

This is a single-variable equation about t_0 and can be numerically solved to obtain t_0. Similarly, by substituting (40) into (28), the new t_{SAT2} can be obtained

$$t_{\text{SAT2}} = \frac{B_{\text{SAT2}} A_{\text{CORE2}} N_4}{V_{\text{LOAD}}} \left(1 + \frac{2}{\pi}\arctan\sqrt{\frac{A_2\cos(\omega t_0)}{V_{\text{LOAD}}} - 1 - E_2}\right). \tag{42}$$

Following the same steps for the case where the clampable core internally reaches B_{SAT1} first, it can be shown that

$$t_{\text{SAT1}} = \frac{B_{\text{SAT1}} A_{\text{CORE1}} N_4 N_2}{V_{\text{LOAD}} N_3} \left(1 + \frac{2}{\pi}\arctan\sqrt{\frac{A_1\cos(\omega t_0)}{V_{\text{LOAD}}} - 1 - E_1}\right). \tag{43}$$

The t_{tail} value in either case can be obtained via identical procedures used in the previous section.

The newly acquired t_0, t_{SAT}, and t_{tail} will now accurately describe the behavior of the two-core cascade magnetics, even under the non-negligible Δi_g during the saturation window.

D. Nonlinearity Consideration: Parasitic Resistance

Thus far, $V_{\text{core}}(t)$ has been ignoring any parasitic voltage development other than the main load voltage presented through an ideal rectifier. There are many situations that can cause a significant deviation from such a case (e.g., high current level, high winding resistance, and low load voltage). The KVL must be updated in these situations to reflect a correct flux balance [23]. Otherwise, t_{SAT}, which is based on this flux balance, is overestimated. Denoting $V_R(t)$ as the lumped parasitic voltage development referred to the secondary side of the ungapped core, (12) in these scenarios must be updated to

$$2B_{\text{SAT2}} A_{\text{CORE2}} N_4 = \int_{t_{\text{tail}}}^{t_0} V_{\text{tail}}(t)\mathrm{d}t + V_{\text{LOAD}} t_{\text{SAT2}} + \int_{t_0}^{t_0 + t_{\text{SAT2}}} V_R(t)\mathrm{d}t. \tag{44}$$

Here, the lumped voltage, $V_R(t)$, which is defined as $V_R(t) = V_{\text{core}}(t) - V_{\text{LOAD}}$, is demonstrated with a winding resistance, R_{winding}, that can be measured in the lab. However, it can be readily expanded to include voltage drops due to a nonideal rectifier. Please note that here considers the case where $t_{\text{SAT}} = t_{\text{SAT2}}$ for demonstration.

According to the KVL on the load side

$$\begin{aligned} V_{\text{core}}(t) &= R_{\text{winding}}\left(i'_S(t) - i'_g(t)\right) + V_{\text{LOAD}} \\ &= R_{\text{winding}} \cdot \frac{N_1 N_3 I_P}{N_2 N_4}\sin(\omega t) + V_{\text{LOAD}} \\ &\quad - R_{\text{winding}}\left(i'_g(t_0) + \frac{N_3^2}{N_4^2 L_g}\int_{t_0}^{t} V_{\text{core}}(t)\mathrm{d}t\right). \end{aligned} \tag{45}$$

Here, $i'_S(t)$ and $i'_g(t)$ are $i_S(t)$ and $i_g(t)$ referred to the secondary side of the ungapped core, respectively, where $i_S(t) = N_1/N_2 \cdot I_P\sin(\omega t)$ and $i_g(t)$ is defined in (9). The circuit model with currents referred to the secondary side of the ungapped core is presented in Fig. 6.

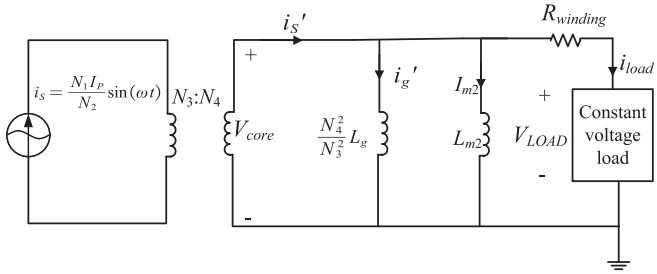

Fig. 6. Equivalent circuit model with parasitic resistance.

For the evaluation of (45), $i'_g(t_0)$ needs to be computed first. It can be done by plugging (40) into (13), evaluating it at $t = t_0$, and referring it to the load side. The result is

$$\begin{aligned} i'_g(t_0) &= -\frac{B_{\text{SAT2}} A_{\text{CORE2}} N_3^2}{L_g N_4} + \frac{N_3^2}{L_g N_4^2}\int_{t_{\text{tail}}}^{t_0} V_{\text{tail}}(\tau)d\tau \\ &= -\frac{2B_{\text{SAT2}} A_{\text{CORE2}} N_3^2}{\pi L_g N_4}\arctan\sqrt{\frac{A_2\cos(\omega t_0)}{V_{\text{LOAD}}} - 1 - E_2}. \end{aligned} \tag{46}$$

Solving the first-order differential equation, (45), with respect to $V_{\text{core}}(t)$ and performing a linear shift of $-V_{\text{LOAD}}$ yields $V_R(t) =$

$V_{\text{core}}(t) - V_{\text{LOAD}}$

$$V_R(t) = V_{\text{core}}(t) - V_{\text{LOAD}} = \frac{GK^2\omega\cos(\omega t) + GK\omega^2\sin(\omega t)}{K^3 + K\omega^2} \quad (47)$$

where

$$G = \frac{R_{\text{winding}} N_1 N_3 I_P}{N_2 N_4} \text{ and } K = \frac{R_{\text{winding}} N_3^2}{N_4^2 L_g}. \quad (48)$$

Finally, this explicit solution of $V_R(t)$ can be substituted into the flux balance equation, (44), to numerically calculate t_{SAT2} that is corrected for the existence of the significant parasitic voltage development along the current path.

Although this subsection demonstrates the case where $t_{\text{SAT}} = t_{\text{SAT2}}$, it can be shown for the other case (i.e., $t_{\text{SAT}} = t_{\text{SAT1}}$) that the expression for $V_R(t)$ and the values of G and K are identical. Once $V_R(t)$ for $t_{\text{SAT}} = t_{\text{SAT1}}$ is obtained, t_{SAT1} can be computed via the following flux balance equation:

$$\frac{2B_{\text{SAT1}}A_{\text{CORE1}}N_4N_2}{N_3} = \int_{t_{\text{tail}}}^{t_0} V_{\text{tail}}(t)\mathrm{d}t + V_{\text{LOAD}}t_{\text{SAT1}} + \int_{t_0}^{t_0+t_{\text{SAT1}}} V_R(t)\mathrm{d}t. \quad (49)$$

With these t_{SAT1} and t_{SAT2} values that reflect the correct flux balance, the same $\min$ function, (35), will produce the final t_{SAT} for the accurate power calculation. The deviation in flux accumulation due to parasitic resistance is caused by the load current that only conducts during the transfer window. Therefore, t_0 and t_{tail}, which primarily rely on the material characteristics rather than the load/circuit description, do not need to be recalculated.

E. Calculation of the Harvested Power

The cyclic average of the harvested power at the load is simply

$$P_{\text{LOAD}} = \frac{2}{T}\int_{t_0}^{t_0+t_{\text{SAT}}} V_{\text{LOAD}} \cdot i_{\text{load}}(t)\mathrm{d}t. \quad (50)$$

However, as evidenced in Fig. 5, $i_{\text{load}}(t)$ is highly nonlinear and its explicit expression is quite cumbersome to work out. Also, as reflected in the range of this integral, the power is only harvested during the transfer window, adding complexity to the calculation. A numerical solver can be used to directly calculate $i_{\text{load}}(t)$ and finish the integration. However, a top–down method will be demonstrated in this article to calculate P_{LOAD}, utilizing a sinusoidal, secondary side transformer current of the ungapped core. First, all the elements in the middle circuit of Fig. 4 are referred to the secondary side of the ungapped core, creating an equivalent circuit model shown in Fig. 6. Then, P_{LOAD} can be alternatively written as

$$P_{\text{LOAD}} = \frac{2}{T}\int_{t_0}^{t_0+t_{\text{SAT}}} V_{\text{LOAD}} \cdot \left[i'_S(t) - i'_g(t) - I_{m2}(t)\right]\ \mathrm{d}t \quad (51)$$

where $i'_S(t) = \frac{N_1N_3I_P}{N_2N_4}\sin(\omega t)$. Then, it can be organized as

$$P_{\text{LOAD}} = \left[\frac{2}{T}\int_{t_0}^{t_0+t_{\text{SAT}}} V_{\text{LOAD}} \cdot i'_S(t)\ \mathrm{d}t\right] - P_g - P_{m2} = \frac{N_1N_3I_PV_{\text{LOAD}}}{\pi N_2N_4}\left[\cos(\omega t_0) - \cos\left(\omega\left(t_0 + t_{\text{SAT}}\right)\right)\right] - P_g - P_{m2} \quad (52)$$

where P_g is the power supplied to the load-reflected air gap inductance and P_{m2} is the power supplied to the magnetizing inductance of the ungapped core during the transfer window. These power values are individually calculated in the sections below. Although an ideal rectifier is assumed and omitted from Fig. 6 between R_{winding} and the load, an additional loss due to the rectifier (e.g., $\overline{V_{\text{rectifier}}(t) \cdot i_{\text{load}}(t)}$) can be modeled in and subtracted from (52).

1) P_g – Power Supplied to the Reflected air gap Inductance: According to (52) and (9) converted to the load side

$$P_g = \frac{2}{T}\int_{t_0}^{t_0+t_{\text{SAT}}} V_{\text{LOAD}} \cdot i'_g(t)\mathrm{d}t = \frac{2V_{\text{LOAD}}}{T}\int_{t_0}^{t_0+t_{\text{SAT}}}\left(i'_g\left(t_0\right) + \frac{N_3^2V_{\text{LOAD}}\left(t-t_0\right)}{N_4^2L_g}\right)\mathrm{d}t = \frac{2i'_g\left(t_0\right)V_{\text{LOAD}}t_{\text{SAT}}}{T} + \frac{N_3^2V_{\text{LOAD}}^2t_{\text{SAT}}^2}{N_4^2L_gT} \quad (53)$$

where $i'_g(t_0)$ is given in (46) for the case of $t_{\text{SAT}} = t_{\text{SAT2}}$.

In the other case, where $t_{\text{SAT}} = t_{\text{SAT1}}$, it can be shown that (46) changes to

$$i'_g\left(t_0\right) = -\frac{2B_{\text{SAT1}}A_{\text{CORE1}}N_3N_2}{\pi L_gN_4}\arctan\left(\sqrt{\frac{A_1\cos(\omega t_0)}{V_{\text{LOAD}}} - 1 - E_1}\right) \quad (54)$$

These values are plugged into (53) to finish the calculation of average P_g during the power transfer window. The instantaneous P_g in reality will be dynamically and continuously changing no matter which core saturates first. However, the average P_g will be largely unchanged once field-related variables are decided.

2) P_{m2} – Power Supplied to the Magnetizing Inductance of the Ungapped Core: Assuming an effective design with a relatively low voltage drop across R_{winding} compared to V_{LOAD}, P_{m2}, the integration of $V_{\text{LOAD}} \cdot I_{m2}(t)$ can be approximated to the integration of $V_{\text{core}}(t) \cdot I_{m2}(t)$

$$P_{m2} = \frac{2}{T}\int_{t_0}^{t_0+t_{\text{SAT}}} V_{\text{LOAD}} \cdot I_{m2}(t)\mathrm{d}t \approx \frac{2}{T}\int_{t_0}^{t_0+t_{\text{SAT}}} V_{\text{core}}(t) \cdot I_{m2}(t)\mathrm{d}t \approx \frac{2A_{\text{CORE2}}\,l_{m2}}{T}\int_{B_2(t_0)}^{B_2(t_0+t_{\text{SAT2}})} H_2\ \mathrm{d}B_2, \quad (55)$$

where H_2 can be obtained by rearranging (17) as follows:

$$H_2 = \frac{2B_{\text{SAT2}}}{\mu_{r2}\mu_0\pi} \cdot \tan\left(\frac{\pi}{2} \cdot \frac{B_2}{B_{\text{SAT2}}}\right). \tag{56}$$

By combining (55) and (56) and finishing the integration, P_{m2} can be calculated as

$$P_{m2} = \frac{2A_{\text{CORE2}}l_{m2}}{T}\frac{4B_{\text{SAT2}}^2}{\mu_{r2}\mu_0\pi^2}\ln\left(\frac{\cos\left(\frac{\pi B_2(t_0)}{2B_{\text{SAT2}}}\right)}{\cos\left(\frac{\pi B_2(t_0+t_{\text{SAT2}})}{2B_{\text{SAT2}}}\right)}\right). \tag{57}$$

To evaluate $B_2(t_0)$ and $B_2(t_0 + t_{\text{SAT2}})$, the KCL at the top node on the load side in Fig. 6 is considered

$$i'_S(t) = i'_g(t) + I_{m2}(t) + i_{\text{load}}(t). \tag{58}$$

At the beginning and end of the transfer window, the load current must be negligibly small due to saturation (i.e., $i_{\text{load}}(t_0) = 0$ and $i_{\text{load}}(t_0 + t_{\text{SAT}}) = 0$). At these time points

$$I_{m2}(t_0) = \frac{N_1N_3I_P}{N_2N_4}\sin(\omega t_0) - i'_g(t_0) \tag{59}$$

and

$$I_{m2}(t_0 + t_{\text{SAT2}}) = \frac{N_1N_3I_P}{N_2N_4}\sin(\omega(t_0 + t_{\text{SAT2}})) - i'_g(t_0 + t_{\text{SAT2}}). \tag{60}$$

Here, $i'_g(t_0 + t_{\text{SAT2}})$ can be obtained via evaluating (9) at $t = t_0 + t_{\text{SAT2}}$ and referring it to the load side. When combined and organized, it can be shown

$$i'_g(t_0 + t_{\text{SAT2}}) = i'_g(t_0) + \frac{N_3^2V_{\text{LOAD}}t_{\text{SAT2}}}{N_4^2L_g}. \tag{61}$$

Using (21) with the values of $i'_g(t_0)$, $i'_g(t_0 + t_{\text{SAT2}})$, $I_{m2}(t_0)$, and $I_{m2}(t_0 + t_{\text{SAT2}})$, calculated in (46), (61), (59), and (60), respectively, $B_2(t_0)$ and $B_2(t_0 + t_{\text{SAT2}})$ can be evaluated

$$B_2(t_0) = \frac{2B_{\text{SAT2}}}{\pi}\arctan\left(\frac{\mu_{r2}\mu_0\pi}{2B_{\text{SAT2}}} \cdot \frac{N_4I_{m2}(t_0)}{l_{m2}}\right) \tag{62}$$

and

$$B_2(t_0 + t_{\text{SAT2}}) = \frac{2B_{\text{SAT2}}}{\pi}\arctan\left(\frac{\mu_{r2}\mu_0\pi}{2B_{\text{SAT2}}} \cdot \frac{N_4I_{m2}(t_0 + t_{\text{SAT2}})}{l_{m2}}\right). \tag{63}$$

Once $B_2(t_0)$ and $B_2(t_0 + t_{\text{SAT2}})$ are evaluated, (57) can be finally calculated to provide P_{m2}.

For the case of $t_{\text{SAT}} = t_{\text{SAT1}}$, nearly identical steps can be followed for the calculation of the power supplied to the magnetizing inductance of the clampable core, P_{m1}. The different procedures are highlighted as follows:

$$I_{m1}(t_0) = \frac{N_1I_P}{N_2}\sin(\omega t_0) - i_g(t_0) \tag{64}$$

$$I_{m1}(t_0 + t_{\text{SAT1}}) = \frac{N_1I_P}{N_2}\sin(\omega(t_0 + t_{\text{SAT1}})) - i_g(t_0 + t_{\text{SAT1}}) \tag{65}$$

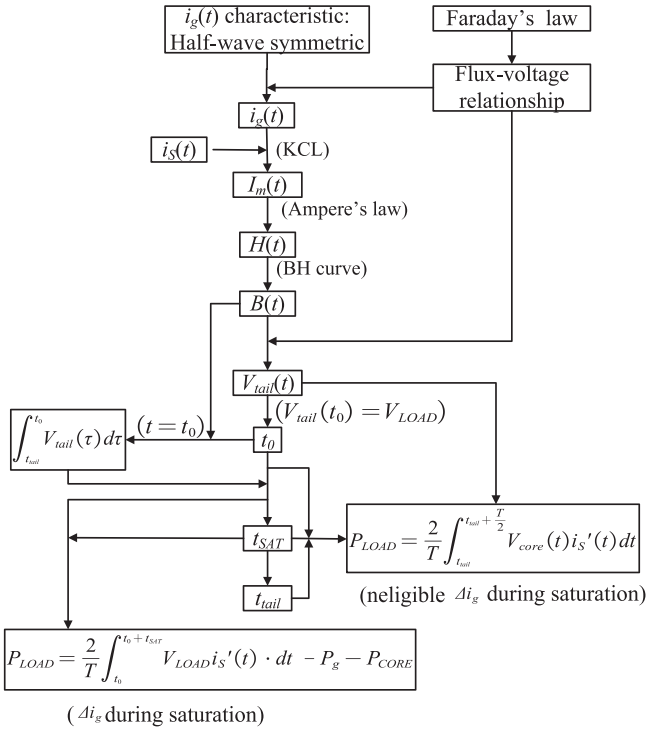

Fig. 7. Flowchart of the mathematical model.

$$B_1(t_0) = \frac{2B_{\text{SAT1}}}{\pi} \cdot \arctan\left(\frac{\mu_{r1}\mu_0\pi}{2B_{\text{SAT1}}} \cdot \frac{N_2I_{m1}(t_0)}{l_{m1}}\right) \tag{66}$$

and

$$B_1(t_0 + t_{\text{SAT1}}) = \frac{2B_{\text{SAT1}}}{\pi} \times \arctan\left(\frac{\mu_{r1}\mu_0\pi}{2B_{\text{SAT1}}} \cdot \frac{N_2I_{m1}(t_0+t_{\text{SAT1}})}{l_{m1}}\right). \tag{67}$$

Then, P_{m1}, which will replace P_{m2} in (52) for this case, is

$$P_{m1} = \frac{2A_{\text{CORE1}}l_{m1}}{T}\frac{4B_{\text{SAT1}}^2}{\mu_{r1}\mu_0\pi^2}\ln\left(\frac{\cos\left(\frac{\pi B_1(t_0)}{2B_{\text{SAT1}}}\right)}{\cos\left(\frac{\pi B_1(t_0+t_{\text{SAT1}})}{2B_{\text{SAT1}}}\right)}\right). \tag{68}$$

F. Power Calculation Flowchart

The steps for the calculation of the average harvested power are summarized in Fig. 7. The right flow path is for the case where the change in the air gap current during the saturation window can be ignored. In this case, Δi_g is negligible and $V_{\text{tail}}(t)$ has an explicit expression. The average load power, then, can be obtained with the multiple current entities referred to the load side and the voltage across the ungapped core directly. Please note $V_{\text{core}}(t)$ is: $V_{\text{tail}}(t)$ from t_{tail} to t_0; V_{LOAD} from t_0 to $t_0 + t_{\text{SAT}}$; and zero elsewhere.

TABLE I
CORE PARAMETERS

Parameter	Clampable core	Ungapped core
Type	VAC-W158	VAC-W424
Magnetic path length	34.2 cm	10.2 cm
Air gap length	0.0255 mm	0 mm
Cross-sectional area	6.2 cm^2	0.86 cm^2
Height	31.6 mm	18.5 mm
Permeability	13,400	282,000
Maximum flux density	0.9 T	1.2 T
Core material	VITROPERM $Fe_{73.5}Cu_1Nb_3Si_{15.5}B_7$	

The flow path on the left is for the case where Δi_g is not negligible. For this case, explicit expressions of $V_{\text{tail}}(t)$ and t_{tail} are not necessary for the calculation of the average harvested power. However, the power supplied to the reflected air gap inductance and magnetizing inductance, and starting point and duration of the transfer window must be calculated.

This power calculation flowchart is for the two-core structure consisting of a clampable core in tandem with an ungapped, high-permeability core and feeding a realistic, constant voltage load. The high-permeability core eliminates the necessity of the impedance matching between the ungapped core and the load. When the core is not saturated, the core with an extremely high permeability provides orders of magnitude larger shunt impedance than a constant voltage load, which must be very low impedance in principle (ideally zero), forcing most of the transformer current to flow into the load. After the transfer window closes due to the core saturation, the shunt impedance approaches zero. However, since no power is delivered to the load during saturation, impedance matching is still unnecessary.

IV. SIMULATION AND EXPERIMENT RESULTS

A. Parameter Estimation and Core Information

For the validation of the mathematical model, VAC-W158 and VAC-W424 are chosen as the clampable and ungapped magnetic cores, respectively. Detailed information on these cores is summarized in Table I, based on manufacturer's datasheet and our in-lab measurement.

The primary and secondary winding turns of the clampable core, N_1 and N_2, are fixed at 2 and 78 turns, respectively. The winding turns of the ungapped core, N_3 and N_4, are fixed at 50 and 108 turns, respectively. The winding resistance on the load side is measured to be 2 Ω at room temperature and considered in the simulation and calculation.

The clampable core consists of two U-shaped cores. The length of the air gap is determined by $l_g = \frac{l_m}{\mu}$, where the magnetic path length of the core, l_m, is obtained from the datasheet of the core and the permeability, μ, is obtained by a lab-measured B–H curve. The saturation flux density, B_{SAT}, is also extracted from the measured B–H curve. Other parameters are obtained from the datasheets of the magnetic cores used.

B. Simulation Details

In our simulation, a dc voltage source is used for the constant voltage load, which is connected to the ungapped magnetic core through a diode bridge rectifier, as shown in Fig. 8. Each diode has a forward voltage drop of 0.12 V in the simulation circuit. The simulation is performed on LTspice with two different ac current amplitudes of $I_P = 4.7$ A and 7 A, and at three different operating frequencies: 60 Hz; 120 Hz; and 180 Hz. L_{m1} and L_{m2} are modeled as nonlinear inductances in LTspice with flux descriptions provided in (21), which include periodically saturating behaviors of the magnetic cores. The simulation results are provided in Figs. 11 and 12. For convenience, these are overlaid with the calculation results based on the modeling of the previous sections and experimental results of the next section.

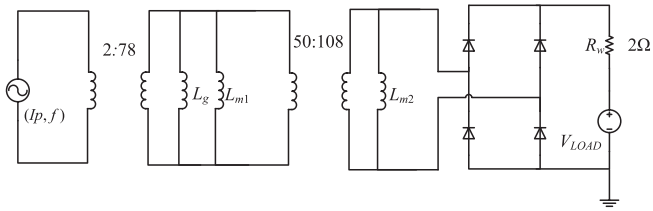

Fig. 8. Simulation circuit.

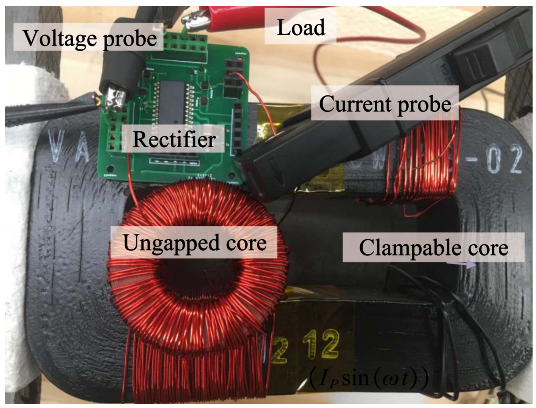

Fig. 9. Detailed experimental setup.

C. Experiment Details and Results of Load Power

To verify the model of the cascaded cores for electromagnetic EH, six experiments are performed with the same settings used for the simulation (i.e., two primary current amplitudes in combination with three line frequencies). The detailed experimental setup is shown in Fig. 9 and overall experimental setup is shown in Fig. 10. An adequately loaded dc voltage supply is used as the constant voltage load. Four power resistors of 2.2 Ω each are used to create the primary current and provide the magnetic field that our harvester extracts energy from.

The list of testing equipment used in the experiment is: BK9832 (ac power supply), CPX400S (dc voltage source), MSO64 (oscilloscope), TPP1000 (voltage probe), and TCP0030 A (current probe).

The peak amplitude of the primary source current, I_P, is set to either 4.7 A or 7 A at 60 Hz in the first experiment. The load voltage is swept between 1 V and 6 V. In the next experiment, the frequency of the source current is increased to 120 Hz and the load voltage is swept from 1 V to 8 V. In the last experiment,

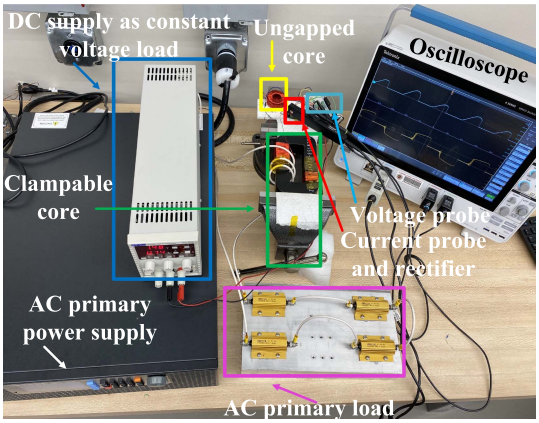

Fig. 10. Overall experimental setup.

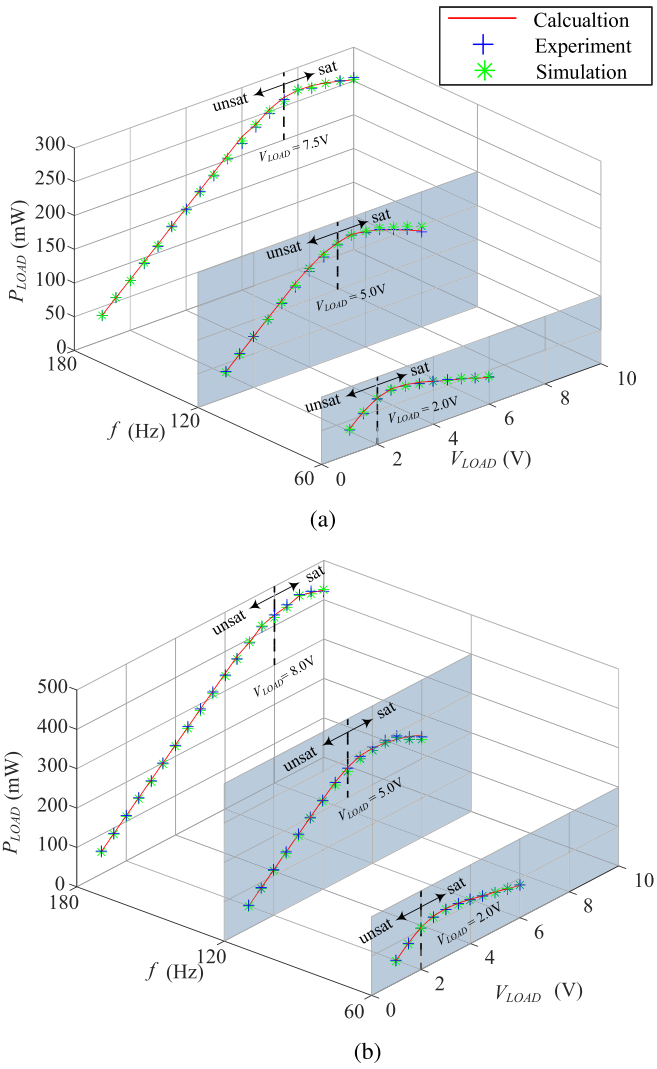

Fig. 11. Harvested power versus load voltage and frequency. (a) Harvested power ($I_P = 4.7$ A). (b) Harvested power ($I_P = 7$ A).

the frequency of the source current is increased to 180 Hz and the load voltage is swept from 1 V to 10 V. Note that a higher load voltage is required to saturate the core at a higher frequency.

Fig. 11 shows the relationship between the average harvested power, P_{LOAD}, and the load voltage, V_{LOAD}. The average harvested power curves are obtained from experiments (blue cross), simulations (green star), and proposed mathematical model (red solid) based on (52). The parameters are listed in Section IV-A. In Fig. 11(a), where $I_P = 4.7$ A, the maximum harvested power is 74 mW for $f = 60$ Hz at $V_{\mathrm{LOAD}} = 2.5$ V, 175 mW for $f = 120$ Hz at $V_{\mathrm{LOAD}} = 5.5$ V, and 266 mW for $f = 180$ Hz at $V_{\mathrm{LOAD}} = 8$ V. In Fig. 11(b), where $I_P = 7$ A, the maximum harvested power is 120 mW for $f = 60$ Hz at $V_{\mathrm{LOAD}} = 2.5$ V, 295 mW for $f = 120$ Hz at $V_{\mathrm{LOAD}} = 6$ V, and 445 mW for $f = 180$ Hz at $V_{\mathrm{LOAD}} = 9$ V. In each curve, the critical point where the core starts entering magnetic saturation is marked with vertical black lines. Below that critical V_{LOAD} level (i.e., left of the vertical black lines), the core is completely free of saturation for the whole cycle and a near-ideal current transformer shows a highly linear response. The maximum harvested power points (i.e., peaks) are clearly located inside the saturation regions (i.e., right of the vertical black lines) for all cases.

Fig. 11 shows that the maximum harvested power increases as the source current and frequency increase. This is an intuitive result in general in that the magnetic field in the magnetic cores is strengthened by the increased current and that the ratio of the transfer window over a half cycle gets larger with the increased frequency. Note that the demonstrated in this article is a relatively low frequency range. If the energy harvester is coupled with a primary system carrying a current with a much higher frequency, more factors should be considered (e.g., skin and proximity effects) for more accurate estimation. An interesting point is that the actual peak points of these curves—the maximum harvested power points—occur when the cores are slightly saturated. When V_{LOAD} is small, the magnetic flux density in the core may not reach B_{SAT} in a half cycle. In this case, as the core is never saturated (i.e., $t_{\mathrm{SAT}} = T/2$), the magnetic stage is essentially a regular current transformer that outputs a constant current regardless of the load condition. Therefore, the graphs remain strongly linear with V_{LOAD} until the saturation points. On the other hand, if the magnetic flux density in the core can reach B_{SAT} within a half cycle, a higher load voltage reduces the length of the transfer window, t_{SAT}, which in turn leads to a lower average load current. An increasing load voltage and decreasing load current contend each other for power calculation. Initially, the power gain due to the increasing load voltage outpaces the power loss due to the lower average current, enhancing the overall harvested power. This is because the transfer window shrinks from the current's zero crossing points. However, as the source current increases toward its peak, the loss in current overtakes the gain in voltage, driving the total harvested power down. Therefore, the harvested power is maximized when the core is allowed to saturate rather "softly." Controlling the level of saturation of the core is crucial to harvest the maximum magnetic energy from a sinusoidal primary current. Note that this analysis is true under passive rectification and is subject to change if an elaborate rectification strategy is employed.

Fig. 12 shows the error of the average harvested power obtained from the mathematics model and simulation, with respect

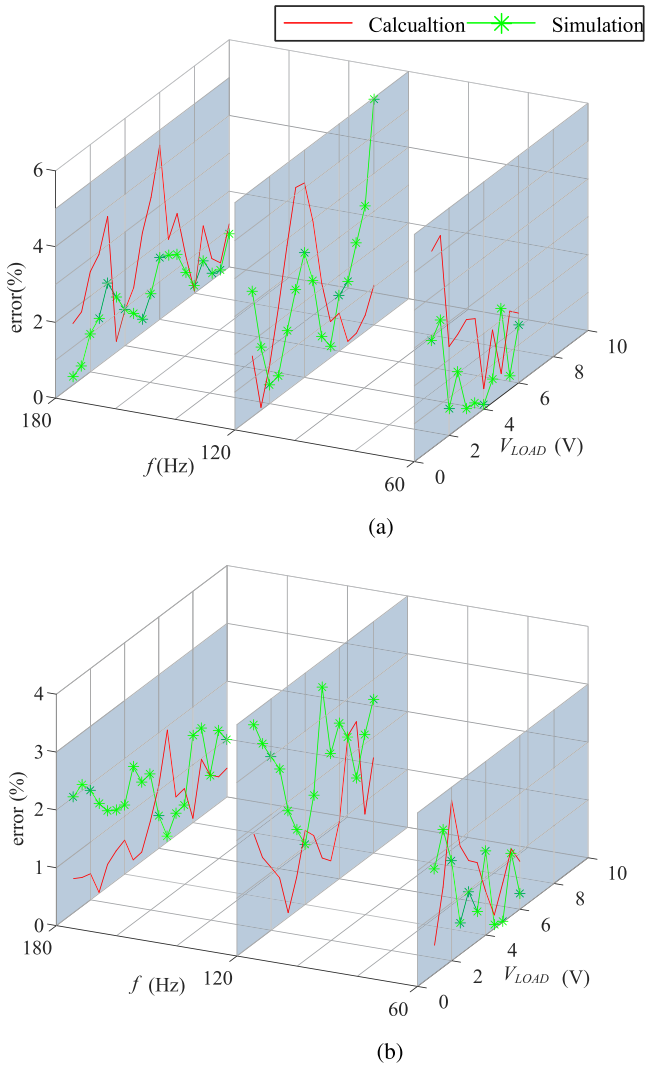

Fig. 12. Error plots for the calculation and simulation. (a) Error plot for $I_P = 4.7$ A. (b) Error plot for $I_P = 7$ A.

to the experiments. As shown in Figs. 11 and 12, the load power obtained from the calculation, simulation, and experiments are in excellent agreement and the error is under 6% for all the cases. The error is primarily due to the approximation of the B–H curve as an arctan function. With a more elaborate and accurate construction of the actual B–H curve, the model accuracy will be improved. The model accuracy can also be enhanced with the increasing level of details of the modeled parasitics (e.g., beyond winding resistance). However, these enhancements in the model accuracy will be in a direct tradeoff relationship with the calculation complexity and simulation time.

Fig. 13 represents the time-domain comparisons of the mathematical model, LTspice simulation, and experiment. The load current and core voltage waveforms at 60 Hz are provided for three different levels of magnetic saturation: unsaturated; soft saturated; and hard saturated. In all cases, the waveforms of the calculation model, simulation, and experiment show excellent agreement, validating the accuracy of our model.

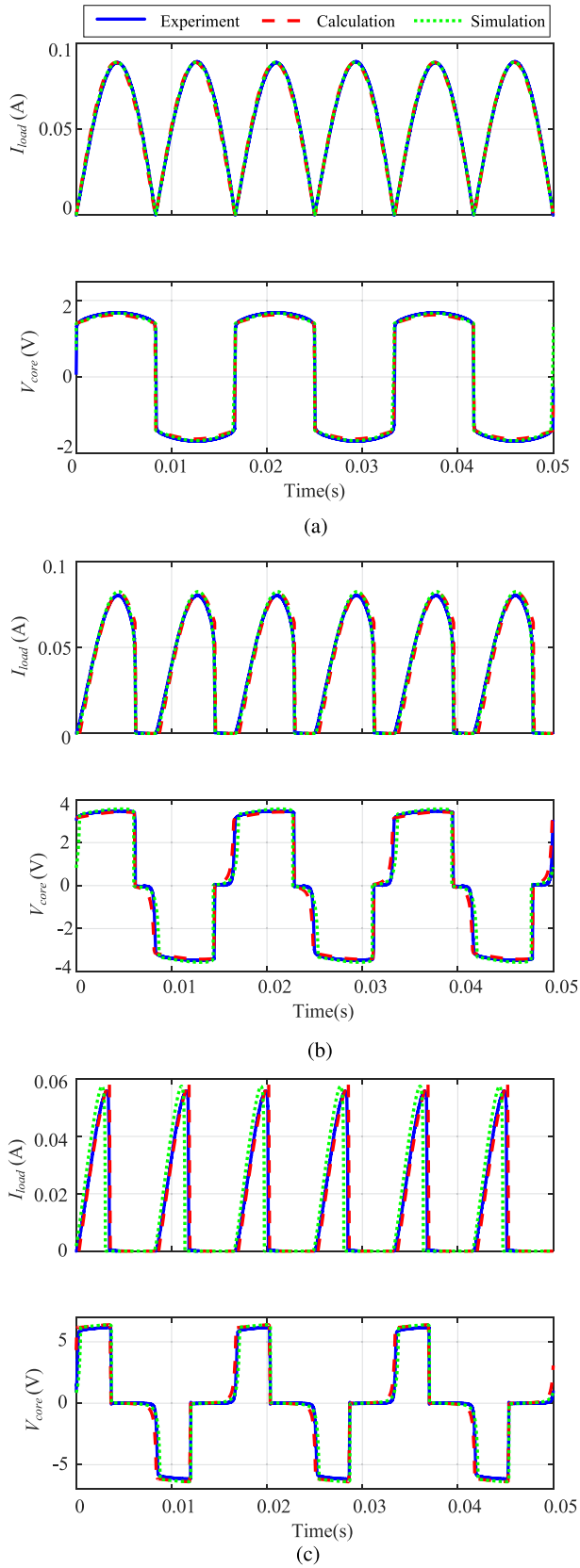

Fig. 13. Experimental waveforms of load current and core voltage ($I_P = 7$ A, $f = 60$ Hz). (a) Nonsaturation – $V_{\mathrm{LOAD}} = 1.3$ V. (b) Soft saturation – $V_{\mathrm{LOAD}} = 3$ V. (c) Hard saturation – $V_{\mathrm{LOAD}} = 6$ V.

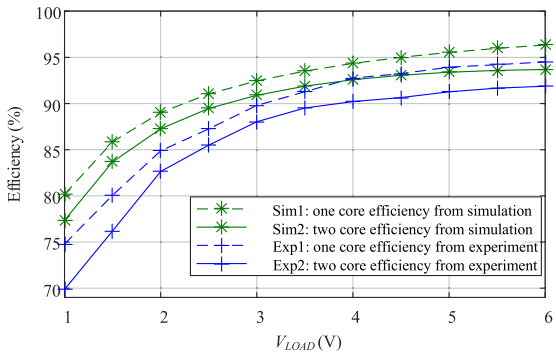

Fig. 14. Efficiency versus load voltage.

Fig. 14 shows the efficiency of the proposed energy harvester with cascaded magnetics with the primary current, I_P, of 4.7 A at 60 Hz. The green solid line, Sim2, and the blue solid line, Exp2, show the two-core structure efficiency, which is calculated as the load power divided by the input power of the clampable core, obtained from the simulation and experiment, respectively. The input power of the clampable core is measured via the deduction method (i.e., ac primary source power minus ac primary load power). The green dotted line, Sim1, and the blue dotted line, Exp1, show the efficiency of the single-core structure under the identical operating condition. These lines are conveniently provided for a quick comparison to our cascaded structure. For this single-core structure, the efficiency is calculated as the load power divided by the input power of the ungapped core, obtained from the simulation and experiment, respectively. The input power of the ungapped core is directly measured by the primary current and primary voltage of the ungapped core. As shown in Fig. 14, the energy harvester efficiency increases when the load voltage increases. This is highly expected because as the core is driven to harder saturation (i.e., higher V_{LOAD}), the average current drops in response to the increasing voltage, naturally lowering the I^2R conduction loss in wiring, which is the dominant loss mechanism in our harvester. The efficiency degradation is less than 3% between the single-core and two-core structures at the likely operating point with the maximum harvest at $V_{\mathrm{LOAD}} = 2.5$ V. As it can be inferred from high V_{LOAD} points, the efficiency of our harvester will readily reach 95%+ by simply replacing the windings with thicker wire.

V. Conclusion

This article presents a cascaded two-core magnetic structure for ac-driven electromagnetic EH. The structure consists of a clampable core and an ungapped high permeability core. The two-core structure enhances the nonintrusiveness of the installation of the energy harvester and guarantees maximum power extraction at the same time. The utilization of the clampable core avoids the downtime of the primary system when installing the ac-driven electromagnetic energy harvester. This can drastically lower the entry barriers in many areas for this technology to be deployed, especially in mission-critical applications. Due to the existence of air gaps in the clampable core and multiple cores in cascaded stages, the mathematical model for the traditional single-core harvester cannot be used to describe the performance of the cascaded two-core structure. This is the first work to introduce mathematical derivations of this structure for the timing characteristics and level of energy extraction. Detailed mathematical derivations and rigorous proof have been demonstrated via simulations and experiments. The accuracy in modeling is greatly enhanced by the inclusion of the tail voltage during the saturation window for the transfer window. Simulation and experiment results illustrate that the proposed modeling method is accurate in the prediction of the harvested power as well as the time-domain waveforms. The harvested power is maximized when the B-field in the ungapped core is allowed to mildly saturate. If the primary power and frequency can be freely controlled, increasing the amplitude of the primary side current and its frequency can directly increase the harvested power.

References

[1] L. Zuo and X. Tang, "Large-scale vibration energy harvesting," *J. Intell. Mater. Syst. Structures*, vol. 24, no. 11, pp. 1405–1430, 2013.
[2] N. Kong and D. S. Ha, "Low-power design of a self-powered piezoelectric energy harvesting system with maximum power point tracking," *IEEE Trans. Power Electron.*, vol. 27, no. 5, pp. 2298–2308, May 2012.
[3] T. Ruan, Z. J. Chew, and M. Zhu, "Energy-aware approaches for energy harvesting powered wireless sensor nodes," *IEEE Sensors J.*, vol. 17, no. 7, pp. 2165–2173, Apr. 2017.
[4] M. A. Andersson, A. Özçelikkale, M. Johansson, U. Engström, A. Vorobiev, and J. Stake, "Feasibility of ambient rf energy harvesting for self-sustainable m2m communications using transparent and flexible graphene antennas," *IEEE Access*, vol. 4, pp. 5850–5857, 2016.
[5] H. Zhang, Y.-X. Guo, Z. Zhong, and W. Wu, "Cooperative integration of RF energy harvesting and dedicated WPT for wireless sensor networks," *IEEE Microw. Wireless Compon. Lett.*, vol. 29, no. 4, pp. 291–293, Apr. 2019.
[6] E. J. Carlson, K. Strunz, and B. P. Otis, "A 20 mV input boost converter with efficient digital control for thermoelectric energy harvesting," *IEEE J. Solid-State Circuits*, vol. 45, no. 4, pp. 741–750, Apr. 2010.
[7] M. Ashraf and N. Masoumi, "A thermal energy harvesting power supply with an internal startup circuit for pacemakers," *IEEE Trans. Very Large Scale Integr. (VLSI) Syst.*, vol. 24, no. 1, pp. 26–37, Jan. 2016.
[8] R. Dayal, K. Modepalli, and L. Parsa, "A new optimum power control scheme for low-power energy harvesting systems," *IEEE Trans. Ind. Appl.*, vol. 49, no. 6, pp. 2651–2661, Nov./Dec. 2013.
[9] Y. Rao and D. P. Arnold, "An input-powered vibrational energy harvesting interface circuit with zero standby power," *IEEE Trans. Power Electron.*, vol. 26, no. 12, pp. 3524–3533, Dec. 2011.
[10] Q. Sun, S. Patil, N.-X. Sun, and B. Lehman, "Inductive magnetic harvester with resonant capacitive rectifier based on synchronized switch harvesting technique," in *Proc. IEEE Energy Convers. Congr. Expo.*, 2013, pp. 4940–4947.
[11] J. Lee and S. W. Yoon, "Optimization of magnet and back-iron topologies in electromagnetic vibration energy harvesters," *IEEE Trans. Magn.*, vol. 51, no. 6, 2015, Art. no. 7208807.
[12] M. Gorlatova, J. Sarik, G. Grebla, M. Cong, I. Kymissis, and G. Zussman, "Movers and shakers: Kinetic energy harvesting for the Internet of Things," *IEEE J. Sel. Areas Commun.*, vol. 33, no. 8, pp. 1624–1639, Aug. 2015.
[13] B. Pekoslawski, P. Krasinski, M. Siedlecki, and A. Napieralski, "Autonomous wireless sensor network for greenhouse environmental conditions monitoring," in *Proc. 20th Int. Conf. Mixed Des. Integr. Circuits Syst.*, 2013, pp. 503–507.
[14] J. Zarate-Roldan, S. Carreon-Bautista, A. Costilla-Reyes, and E. Sanchez-Sinencio, "An ultra-low power power management unit with -40db switching-noise-suppression for a 3×3 thermoelectric generator array with 57% maximum end-to-end efficiency," in *Proc. IEEE Custom Integr. Circuits Conf.*, 2014, pp. 1–4.
[15] D. Altinel and G. K. Kurt, "Modeling of multiple energy sources for hybrid energy harvesting IoT systems," *IEEE Internet Things J.*, vol. 6, no. 6, pp. 10846–10854, Dec. 2019.

[16] S. Kim et al., "Ambient RF energy-harvesting technologies for self-sustainable standalone wireless sensor platforms," *Proc. IEEE Proc. IRE*, vol. 102, no. 11, pp. 1649–1666, Nov. 2014.
[17] M. Kroener, "Energy harvesting technologies: Energy sources, generators and management for wireless autonomous applications," in *Proc. Int. Multi- Conf. Syst., Signals Devices*, 2012, pp. 1–4.
[18] R. Dayal, S. Dwari, and L. Parsa, "A new design for vibration-based electromagnetic energy harvesting systems using coil inductance of microgenerator," *IEEE Trans. Ind. Appl.*, vol. 47, no. 2, pp. 820–830, Mar./Apr. 2011.
[19] H. Wang, Y. Tang, and A. Khaligh, "A bridgeless boost rectifier for low-voltage energy harvesting applications," *IEEE Trans. Power Electron.*, vol. 28, no. 11, pp. 5206–5214, Nov. 2013.
[20] L. Yu, H. Wang, and A. Khaligh, "A discontinuous conduction mode single-stage step-up rectifier for low-voltage energy harvesting applications," *IEEE Trans. Power Electron.*, vol. 32, no. 8, pp. 6161–6169, Aug. 2017.
[21] J. Moon and S. B. Leeb, "Analysis model for magnetic energy harvesters," *IEEE Trans. Power Electron.*, vol. 30, no. 8, pp. 4302–4311, Aug. 2015.
[22] J. Moon and S. B. Leeb, "Power electronic circuits for magnetic energy harvesters," *IEEE Trans. Power Electron.*, vol. 31, no. 1, pp. 270–279, Jan. 2016.
[23] J. Moon and S. B. Leeb, "Power loss analysis with high primary current in magnetic energy harvesters," in *Proc. IEEE 16th Workshop Control Model. Power Electron.*, 2015, pp. 1–8.
[24] J. Wang and W. Chen, "Output characteristics analysis of energy harvesting current transformer," *IEEE Sensors J.*, vol. 21, no. 20, pp. 22595–22602, Oct. 2021.
[25] Y. Zhuang et al., "Improving current transformer-based energy extraction from ac power lines by manipulating magnetic field," *IEEE Trans. Ind. Electron.*, vol. 67, no. 11, pp. 9471–9479, Nov. 2020.
[26] Z. Liu et al., "A novel method for magnetic energy harvesting based on capacitive energy storage and core saturation modulation," *IEEE Trans. Ind. Electron.*, to be published, doi: 10.1109/TIE.2022.3172777.
[27] Y. Tsunoda et al., "A small-size energy-harvesting electric power sensor for implementing existing electrical appliances into hems," *IEEE Sensors J.*, vol. 16, no. 2, pp. 457–463, Jan. 2016.
[28] T.-C. Huang et al., "120% harvesting energy improvement by maximum power extracting control for high sustainability magnetic power monitoring and harvesting system," *IEEE Trans. Power Electron.*, vol. 30, no. 4, pp. 2262–2274, Apr. 2015.
[29] S. Paul, S. Bashir, and J. Chang, "Design of a novel electromagnetic energy harvester with dual core for deicing device of transmission lines," *IEEE Trans. Magn.*, vol. 55, no. 2, Feb. 2019, Art. no. 8000104.
[30] H. Zhang and A. A. Arkadan, "B–H curve-based model for CT error evaluation," *IEEE Trans. Magn.*, vol. 55, no. 6, Jun. 2019, Art. no. 8001204.
[31] G. Liu and X.-B. Xu, "Improved modeling of the nonlinear B-H curve and its application in power cable analysis," *IEEE Trans. Magn.*, vol. 38, no. 4, pp. 1759–1763, Jul. 2002.
[32] A. Astorino, M. Swaminathan, and G. Antonini, "A new approach for magneto-static hysteresis behavioral modeling," *IEEE Trans. Magn.*, vol. 52, no. 9, Sep. 2016, Art. no. 7301014.

Min Gao (Student Member, IEEE) received the B.S. degree in electrical engineering and aotumation from Wuhan University, Hubei, China, in 2019. She is currently working toward the Ph.D. degree in electrical and computer engineering with Florida State University, Tallahassee, FL, USA.

Her current research interests include cascaded magnetics and energy harvesting.

Lifang Yi (Student Member, IEEE) received the B.S. and M.S. degrees in electrical engineering from Nanjing University of Aeronautics and Astronautics, Nanjing, China, in 2016 and 2019, respectively. She is currently working toward the Ph.D. degree in electrical and computer engineering with Florida State University, Tallahassee, FL, USA.

Her current research interests include precise *in situ* magnetic loss measurement, dc circuit breaker, and capacitive wireless power transfer technology.

Jinyeong Moon (Senior Member, IEEE) received the B.S. degree in electrical engineering and computer science from the Korea Advanced Institute of Science and Technology, Daejeon, South Korea, in 2005, the M.S. degree in electrical engineering from Stanford University, Stanford, CA, USA, in 2007, and the Ph.D. degree in electrical engineering and computer science from the Massachusetts Institute of Technology (MIT), Cambridge, MA, USA, in 2016.

He was with Hynix Semiconductor Inc., Icheon, South Korea, from 2007 to 2011 as a Senior Research Engineer, where he was involved in designing analog, digital, and power circuits for DDR4 SDRAM. He was a Postdoctoral Associate with MIT from 2016 to 2017. He was with Maxim Integrated, North Chelmsford, MA, USA, from 2017 to 2018 as a Member of Technical Staff, where he was involved in high efficiency wide bandgap ac–dc converter projects. He is currently an Assistant Professor in the electrical and computer engineering with Florida State University. His research interests include modeling, design, analysis, and measurement of circuits and systems in the fields of power conversion, energy harvesting, electromagnetics, and renewable energy.

Dr. Moon was a recipient of two grand prizes in the MIT Clean Energy Prize in 2014. He was also a recipient of the Kwanjeong Scholarship and the Hynix Strategic Patent Award. He holds 17 registered U.S. and international patents. He currently serves as an Associate Editor for *Journal of Power Electronics* and the Publication Liaison for IEEE Power Electronics Society's Technical Committee 1.